Study of various strain energy distribution in InGaN/GaN multiple quantum wells

YEN-SHENG LIN
Department of Electrical Engineering, Chinese Naval Academy, No. 669 Chun Hsiao Road, Tsoying, Kaohsiung 813, Taiwan, ROC
E-mail: yslin@mail.can.edu.tw

Published online: 21 April 2006

The formation of In-rich quantum dot structures will induce strain energy in the quantum well layer, forming the clusters and stacking faults influencing the optical properties. Our results showed different QW widths with the formation of various In-rich quantum dot structures and different levels of strain energy. Upon thermal annealing, energy relaxation resulted in the reshaping of quantum dots and hence the changes of optical properties. The results of temperature variations of PL spectral peak, integrated PL intensity and PL decay time showed consistent trends in varying strain energy distribution.

1. Introduction

Quantum-dot-like structures have been observed in InGaN/GaN quantum wells (QWs). Such structures are formed because of the large lattice mismatch between InN and GaN, which will result in potential fluctuations and hence the effect of carrier localization (CL) [1–3]. The method of CL has been widely used for interpreting observed optical behaviors in such compounds, such as the S-shaped temperature dependent variation of photoluminescence (PL) spectral peak [4, 5]. On the other hand, the large lattice mismatch between InGaN wells and GaN barriers leads to significant strains in the well layers. The strain-induced piezoelectric field, which generates the quantum confined Stark effect (QCSE), has also been used for explaining the observed optical phenomena, such as the excitation power dependence of PL spectral peak [6–8]. In this effect, electrons and holes are spatially separated. Hence, radiative transition rate is reduced and PL decay time is elongated [9, 10]. It is expected that both effects of CL and QCSE play certain roles in the photon emission mechanisms of such compounds.

The sizes, shapes, compositions and distributions of the indium-aggregated clusters depend on the nominal indium content of InGaN and the degree of spinodal decomposition [11]. With high-resolution transmission electron microscopy (HRTEM), randomly distributed clusters of indium aggregation and phase-separated InN were widely observed. The cluster structures form potential minimums (called localized states) to trap carriers for efficient photon emission [5, 12–14]. Such indium-aggregated distributions are basically located in the quantum well layers; however, they usually diffuse into barriers, extensively under certain conditions [3]. Since the strain energy will be developed during the growth of InGaN QW layers, the designated QW width becomes a crucial factor in the cluster formation and the consequent photon emission characteristics [15, 16].

It had been reported that post-growth thermal annealing could alter the sizes and distributions of self-organized InAs quantum dots [17, 18]. In InGaN compounds, post-growth thermal annealing processes for changing the cluster structures and their photon emission properties were also reported [19–21]. In one of the previous results, a better confined quantum well structure, i.e., weaker indium out-diffusion, after thermal annealing has been reported [21]. The photoluminescence (PL) intensity was increased with the stronger quantum well confinement effect. Post-growth thermal annealing can provide a means for device manufacturers to tune the photon emission in InGaN compounds, wavelength or to tailor the gain spectrum by changing the size/composition of the quantum-dot-like structures, and change the strain energy distribution of InGaN QWs. The information of thermal annealing is also helpful for crystal growers to design growth procedures. Formation of regularly embedded InGaN or InN quantum dots (QDs) around the designated well layers was observed upon thermal annealing under an appropriate condition [22]. PL intensity was significantly increased with the formation of regular QD structures.

In this paper, we mainly report the changed strain energy distribution of Indium rich QD structures by various QW widths and different amount of thermal annealing.

0022-2461
DOI: 10.1007/s10853-005-5629-x

Continuous PL and time-resolved PL (TRPL) measurements were conducted to show various optical behaviors. High-resolution transmission electron microscopy (HRTEM) images were obtained to demonstrate the variations of microstructures. This paper is organized as follows: In Section 2, sample structures and experimental procedures are discussed. The microstructure analysis and optical properties are briefly reported in Section 3. Finally, conclusions are drawn in Section 4.

2. Experimental procedures

The samples were grown on a c-plane sapphire using metal organic chemical vapor deposition. Following the deposition of 30 nm GaN buffer layer and a 2.3 μm GaN layer, QW structures consisting of five pairs of $In_{0.15}Ga_{0.85}N$ well and 10 nm-thick GaN barrier were grown. Three samples of different well widths at 2, 3, and 4 nm were prepared and referred to as samples w20, w30 and w40, respectively. The growth temperatures were 1010 and 720°C for GaN and InGaN, respectively. As-grown samples were thermally annealed in a quartz tube furnace at different temperatures ranging from 800 to 900°C in nitrogen ambient for 30 m.

XRD measurements were carried out using the K_α radiation of Cu, monochromated with the (111) reflection of Ge single crystal. The composition of $In_xGa_{1-x}N$ could be determined by calculating the lattice spacing from the (0002) Bragg reflection peak, and assuming that Vigard's law was applicable for the InN and GaN systems. The density of threading dislocations (TDs) and surface morphologies were examined with atomic force microscopy (AFM) operating in the tapping mode. The PL measurements were excited with a He-Cd laser (Kimmon) at a wavelength of 325 nm.

A cross-sectional sample was prepared conventionally manner by grinding, dimpling and Ar^+-ion milling with 6 KV, 1 mA and an incident angle of 4°. However due to previous experience with In coating materials, the ion milling step was always carried out with the specimen holder at liquid nitrogen temperature in order to minimize the ion beam damage. The HRTEM investigations were performed with both 200 KeV philips CM 200 and 300 KeV JEM 3010 microscopes, all high-resolution micrographs were taken at Scherzer defocous and the sample was viewed along a [11$\bar{2}$0] zone axis, 300 KeV JEM 3010 microscope equipped with a 2 k × 2 k slow-scan CCD camera and a Gatan Imaging Filter (GIF), respectively. Concerning the EF images, the drift between the two pre-edge and the post-edge image recorded has been created by using the cross correlation algorithm available in the Digital Micrograph software of the GIF. In order to remove the background contribution underneath the ionization edges which are specific for the elements and to obtain elemental maps, two different techniques can be used [23, 24]. The jump-ratio method, where the post-edge image is normalized by dividing it by a pre-edge image has been applied. The resulting elemental maps contain less noise and fewer artifacts [24]. However, they cannot be quantified, but qualitative information on the homogeneity of the elemental depth distribution is possible. The strain energy distribution is calculated by the NCEM Phase Extensions to Digital micrograph.

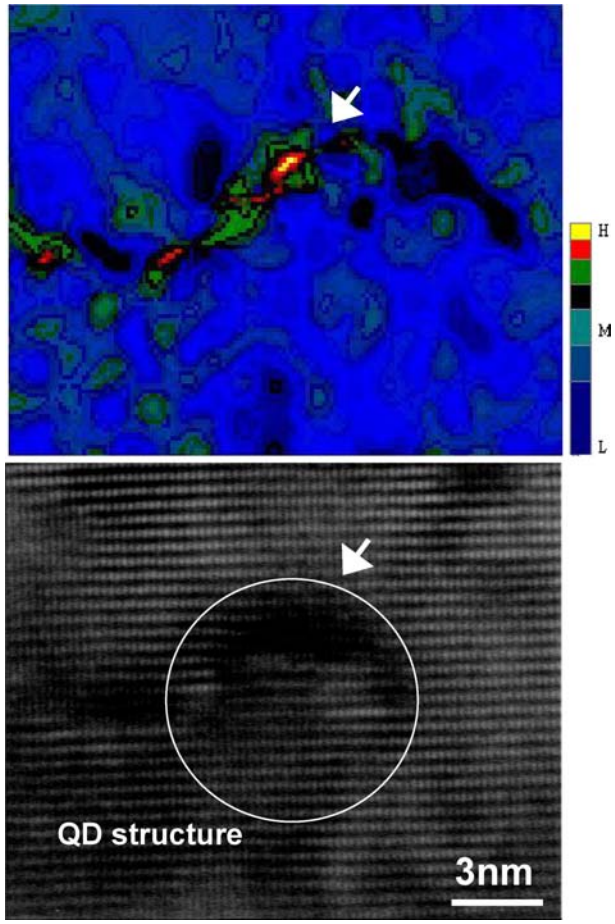

Figure 1 The NCEM Phase Extensions to Digital Micrograph software for calculating strain on QD structure.

3. Results and discussions

We have calculated the strain energy distribution around the QDs, as shown in Fig. 1, in which the higher strain energy is indicated as the white arrow and it will affect the layer structure continuously. In order to know the effect of strain energy in quantum well, grown various QW widths and different thermal annealing treatment were used. Figs 2a–c show the HRTEM images of various QW widths. Due to the higher strain energy built in the QWs layer, the QDs structures are clearly observed on w40 sample. Figs 3a–c show the HRTEM images of 800°C-annealing with various QW widths. In the w30 and W40 samples, contrast spots of irregular sizes and shapes can be seen around the designated QW layers. Certain line features are still quite clear. Although HRTEM images can be affected by the process procedures of HRTEM samples, Fig. 3(b) does show quite a different structure from that in Fig. 3(a), some indium rich clusters that are clearly observed in barriers seem to be the procedures of spinodal decomposition. All

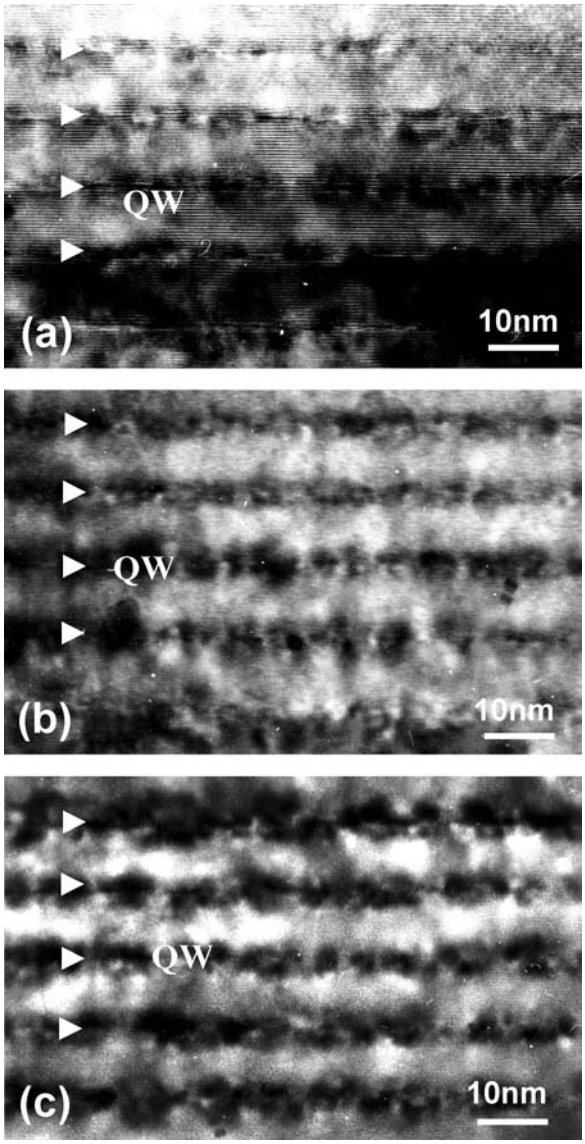

Figure 2 The HRTEM results of InGaN/GaN with (a) 2 nm (b) 3 nm (c) 4 nm QW thickness.

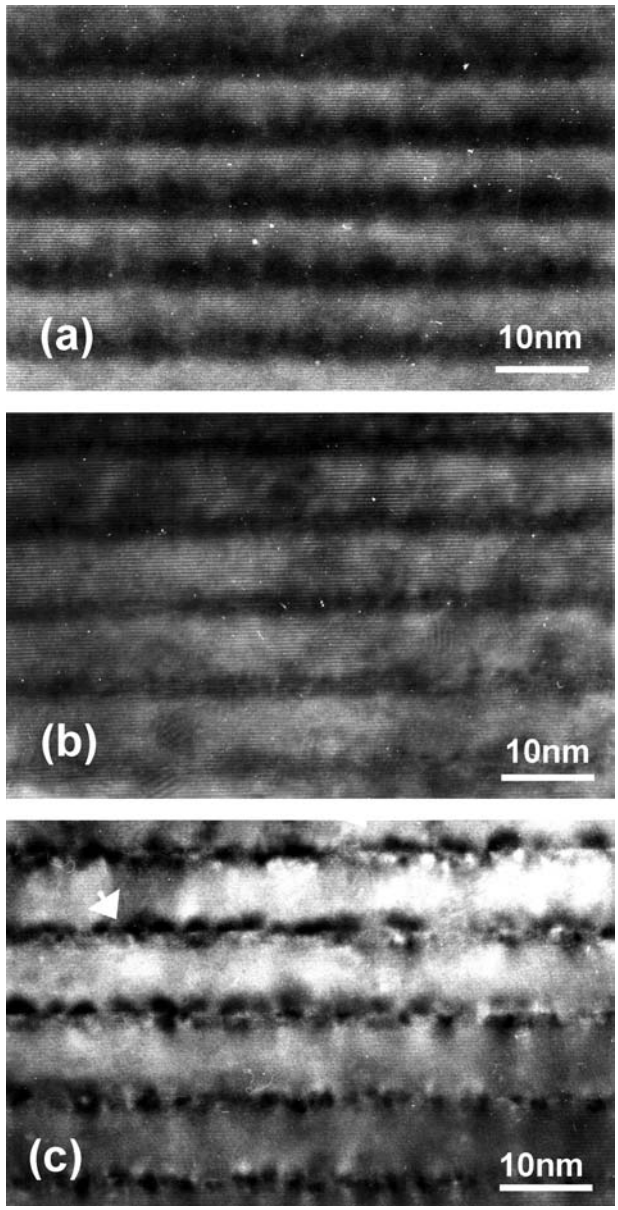

Figure 3 The HRTEM results of InGaN/GaN with 800°C annealing for 30 m, (a) 2 nm (b) 3 nm (c) 4 nm QW thickness.

of them disappear in Fig. 3(c), the high strain energy in the layer must be partially released. High strain energy is expected in w40, and to further provide an evidence of the defects structure in Figs 4a–c, the surface point (V-shape) defects image of the as-grown w20, w30 and w40 samples is shown with atomic force microscopy results. The higher defect density is observed in w40, since the higher strain energy might be relaxed through the formation of thread dislocations or local lattice distortions in the QW layers, and they also led to quite poor photon emission efficiency. Figs 5a–c show the HRTEM images of as-grown, 800°C -annealing and 900°C-annealing w20. The as-grown w20 shows highly irregular and diffusive cluster structures. Clusters diffuse from the designated QW layers into barriers. After thermal annealing at 800°C, cluster structures become much more regular. QDs with sizes of 3–5 nm are quasi-regularly arranged in the designated QW layers. A similar HRTEM image was obtained in a sample of a similar structure under thermal annealing [22]. Energy-filter transmission electron microscopy has been used to identify the existence of coupled QDs.

After thermal annealing, the S-shaped variation of PL peak is maintained in each case. Thermal annealing results in blue shift of PL peak in w20, and red shift in w30 and w40. In all samples, thermal annealing at 800°C leads to the largest spectral shifts. As the thermal annealing temperature increases, the blue shift or red shift is reduced. Fig. 6 shows the temperature-dependent variations of integrated PL intensity of the as-grown and annealed samples. The integrated PL intensities were enhanced upon thermal annealing in w20 and w30 samples, particularly significant in w20. However, that of w40 was reduced. It is interesting to note that the trends in PL peak shifts (blue or red) and integrated PL intensity variations (increase

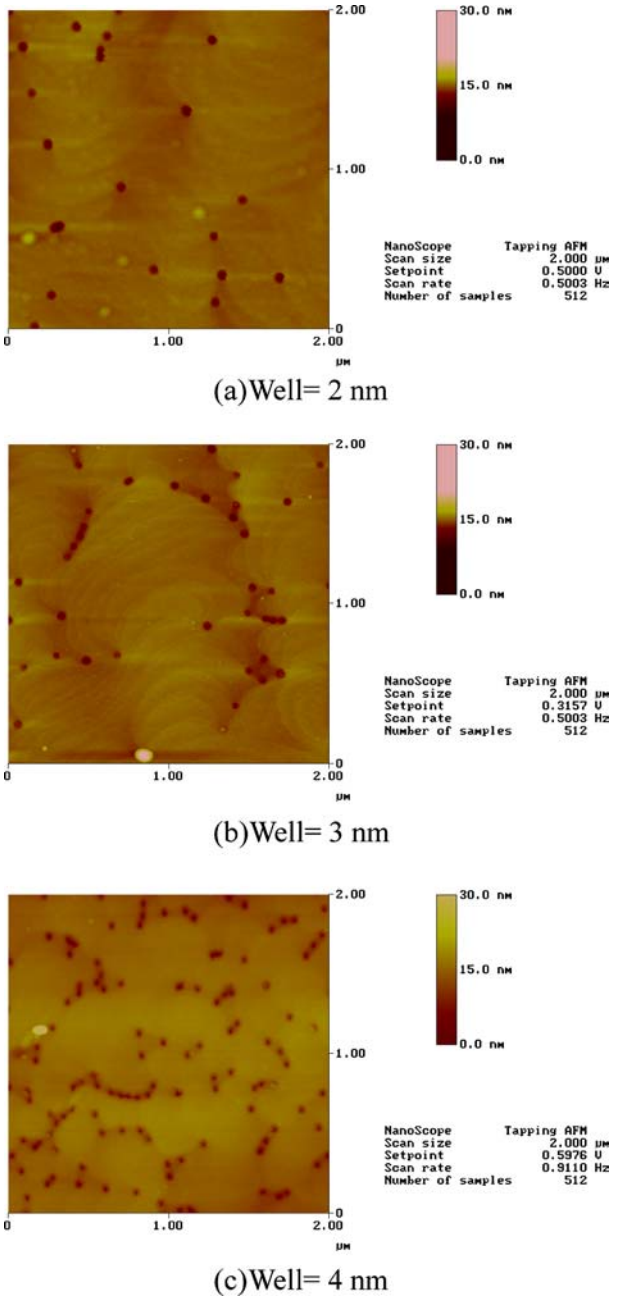

Figure 4 The surface point defects image of the as-grown (a) w20, (b) w30 and (c) w40 samples with atomic force microscopy.

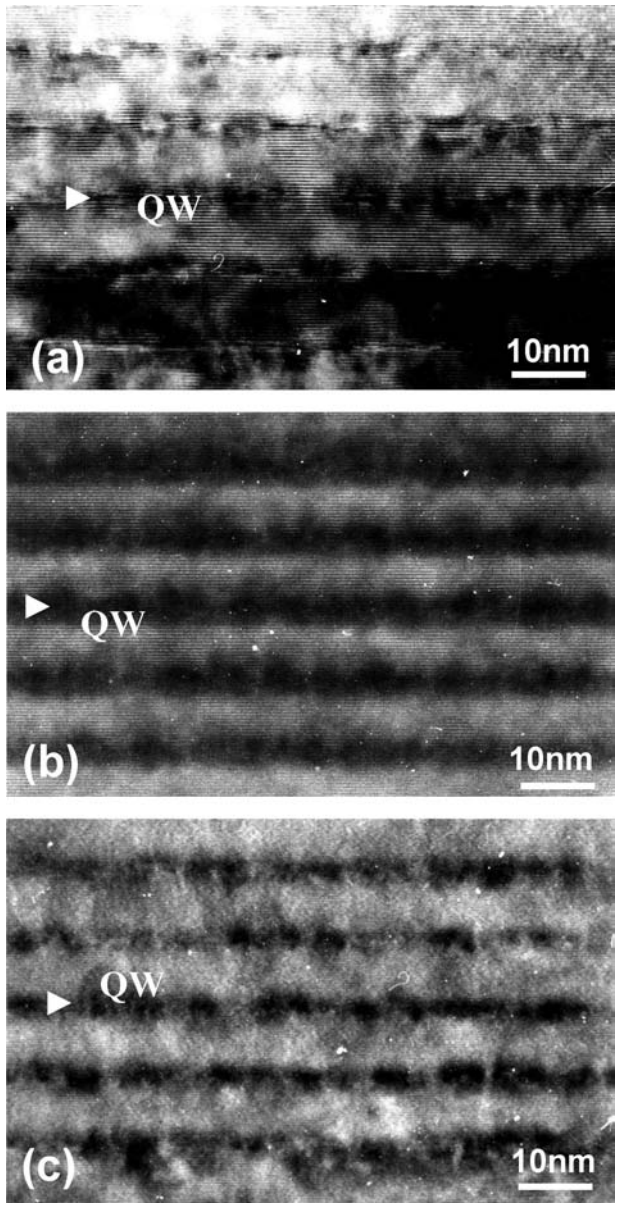

Figure 5 The HRTEM results of InGaN/GaN with 2 nm QW thickness, (a) as-grown, (b) 800°C annealing for 30 min, (c) 900°C annealing for 30 min.

or decrease) with annealing temperature are the same in each of the three samples. As the annealing temperature increases, optical properties generally tend to return to the as-grown condition. However, it is noted that in w20 and w40, the curves of PL peak and integrated PL intensity of 900°C annealing lie between those of 800 and 850°C annealing. Nevertheless, in w30, the curves of 850°C annealing lie between those of 800 and 900°C annealing. This difference indicates different dependencies on annealing temperatures of various samples.

Thermal annealing results in an increase of PL decay times in both samples. In particular, the increase of w20 and w30 occur mainly in the high and low temperature ranges, respectively. The variations in the annealing temperature of these two samples are the same as those of PL spectral peak and integrated PL intensity, as shown in Fig. 6. The as-grown sample of w20 manifests a two-peak feature in the PL decay time variation with temperature. Thermal annealing particularly enhances the peak of higher temperature. On the other hand, the as-grown w30 shows a one-peak feature. The peak was enhanced upon thermal annealing. After thermal annealing of this sample, the time for PL decay become too long to be well calibrated with our measured data.

In w20, upon thermal annealing, spinodal decomposition may dominate the process of relaxing the strain energy built in the well layers. In this process, the "up-hill" diffusion results in the gathering of indium toward their cores, and forms a more regular structure as in Fig. 5(b)

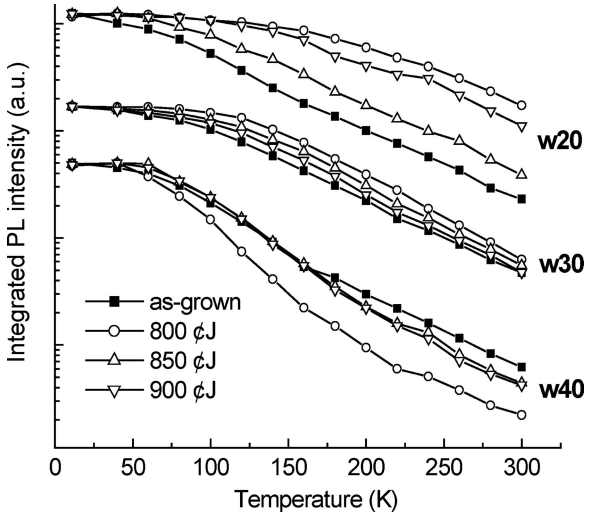

Figure 6 Variations of normalized integrated PL intensities versus temperature of the three samples under various thermally annealing conditions.

[22]. Based on the result, it is concluded that the structure is preferred for enhancing photon emission efficiency from Fig. 6. In w30, upon thermal annealing, more gathering of indium structures appears in barriers and is affected on the distribution of strain energy, the atomic-scale HRTEM images of annealed w30 samples as shown in Fig. 7. However, especially on w40 due to the larger well width leading to larger strain energy, spinodal decomposition becomes less effective [25]. In this situation, the strain energy might be relaxed through the formation of more stacking faults or local lattice distortions upon thermal annealing. Stacking faults and local distortions were easily observed in atomic-scale HRTEM images of annealed w40 samples as shown in Fig. 8. It is speculated that the thermally annealed w40 sample may have a higher density. Such defects exist around clusters and are responsible for the significant decrease in integrated PL intensity with temperature near 50 K, as shown in Fig. 6. Note that in the aforementioned relaxation process of w40, the local strain distribution around a QW may be enhanced although the global stress is reduced. Therefore, the reduction of integrated PL intensity of w40 upon thermal annealing can be

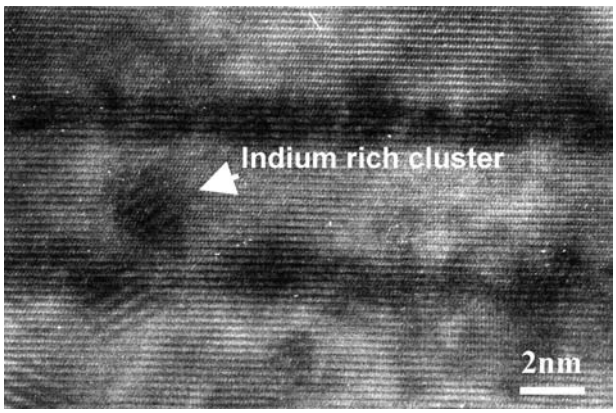

Figure 7 The atomic-scale HRTEM images of annealed w30 samples.

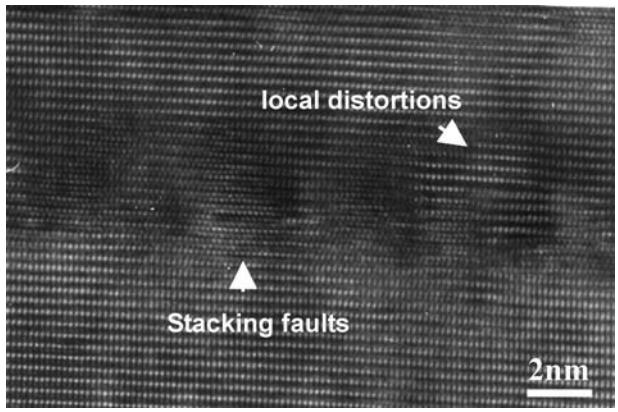

Figure 8 The atomic-scale HRTEM images of annealed w40 samples.

attributed to an increase of either local strain (reduced radiative transition rate due to the enhanced QCSE) or defect density.

The blue shift of PL peak in w20 upon thermal annealing can be attributed to a better quantum confinement. The causes of red shift in w30 and w40 could be quite complicated. They result from the interplay of indium content gathering (red shift trend), quantum confinement (blue shift trend) and strain-induced QCSE (red shift trend). Based on the microstructure observations, the enhanced QCSE may play a key role here. The increasing trends of integrated PL intensities and decay times of w20 upon thermal annealing are consistent. These trends may originate from the mixed effects of the variations of CL and QCSE after thermal annealing. Stronger CL further prevents carriers from non-radiative recombination and hence stronger PL intensities and longer decay times. A weaker QCSE increases the radiative transition rate causing stronger PL intensity. However, it reduces the PL decay time. Since the PL decay time is increased upon thermal annealing, the effect of enhanced CL seems to play the key role in annealed w20 samples. This conclusion is consistent with the well-shaped QDs in annealed w20. It is also consistent with a previous conclusion that CL dominates the optical properties in a thin well sample [26]. In w30, since the red shift of PL peak is quite large and the increase of integrated PL intensity is relatively smaller upon thermal annealing, the enhanced local strain-induced QCSE may dominate over CL in the annealing effects of this sample.

The significant increase of PL decay times at relatively higher temperatures after thermal annealing of w20 implies that CL becomes stronger and defects become less effective in carrier consumption. In w30, upon thermal annealing, the significant increase of decay time at relatively lower temperatures is attributed to stronger CL and enhanced QCSE. Based on the discussions above, the latter may dominate. The extremely long decay time of w40 after thermal annealing is attributed to the enhanced local strain-induced QCSE and hence reduced radiative efficiency.

4. Conclusions

In summary, we have shown the dependencies of optical and material properties of thermally annealed InGaN/GaN QW samples on well width. Due to the higher strain energy observed around the In-rich structures, different distribution of strain energy exists in each sample of different QW widths, and thermal treatment changes again the layer structure. The results of temperature variations of PL spectral peak, integrated PL intensity and PL decay time are consistent with the variation in the annealing temperature. Different variation trends upon thermal annealing in different samples were also consistent with the results of HRTEM images. In our study, after proper thermal treatment, quasi-regular QD structures are able to be observed in different growth procedures, because proper thermal treatment can effectively control the strain energy distribution. As thermal annealing at 800°C of a narrow QW width (2 nm) structure led to regularly distributed QDs and improved optical quality.

Acknowledgment

This research was supported by National Science Council, The Republic of China, under grants NSC 92-2215-E-012-001. The authors gratefully acknowledge Professor Chih-Chung Yang at National Taiwan University for the assistance of optical measurements, Professor Thomas E. Weirich at Aachen University of Technology, Germany and Professor Kung-Jen Ma at Chung Hua University for his fruitful discussions and Dr. Jian-Shihn Tsang at Advanced Epitaxy Technology Inc. Hsinchu Industrial Park, Taiwan for supplying samples.

References

1. Y. NARUKAWA, Y. KAWAKAMI, M. FUNATO, S. FUJITA, S. FUJITA and S. NAKAMURA, *Appl. Phys. Lett.* **70** (1997) 981.
2. M. D. MCCLUSKEY, L. T. ROMANO, B. S. KRUSOR, D. P. BOUR, N. M. JOHNSON and S. BRENNAN, *Ibid.* **72** (1998) 1730.
3. Y. S. LIN, K. J. MA, C. HSU, S. W. FENG, Y. C. CHENG, C. C. LIAO, C. C. YANG, C. C. CHUO, C. M. LEE and J. I. CHYI, *Ibid.* **77** (2000) 2988.
4. T. HINO, S. TOMIYA, T. MIYAJIMA, K. YANASHIMA, S. HASHIMOTO and M. IKEDA, *Ibid.* **76** (2000) 3421.
5. Y. H. CHO, G. H. GAINER, A. J. FISCHER, J. J. SONG, S. KELLER, U. K. MISHRA and S. P. DENBARRS, *Ibid.* **73** (1998) 1370.
6. P. RIBLET, H. HIRAYAMA, A. KINOSHITA, A. HIRATA, T. SUGANO and Y. AOYAGI, *Ibid.* **75** (1999) 2241.
7. S. F. CHICHIBU, A. C. ABARE, M. S. MINSKY, S. KELLER, S. B. FLEISCHER, J. E. BOWERS, E. HU, U. K. MISHRA, L. A. COLDREN, S. P. DENBAARS and T. SOTA, *Ibid.* **73** (1998) 2006.
8. C. K. CHOI, Y. M. KWON, B. D. LITTLE, G. H. GAINER, J. J. SONG and Y. C. CHANG, *Phys. Rev.* **B64** (2001) 245339.
9. R. LANGER, J. SIMON, V. ORITZ, N. T. PELEKANOS, A. BARSKI, R. ANDRÉ and M. GODLEWSKI, *Ibid.* **74** (1999) 3827.
10. P. WALTEREIT, O. BRANDT, A. TRAMPERT, H. T. GRAHN, J. MENNIGER, M. RAMSTEINER, M. REICHE and K. H. PLOOG, *Nature* **406** (2000) 865.
11. I. H. HO and G. B. STRINGFELLOW, *Appl. Phys. Lett.* **69** (1996) 2701.
12. S. CHICHIBU, T. AZUHATA, T. SODA and S. NAKAMURA, *Ibid.* **69** (1996) 4188.
13. S. CHICHIBU, T. AZUHATA, T. SOTA and S. NAKAMURA, *Ibid.* **70** (1997) 2822.
14. M. S. MINSKY, S. B. FLEISCHER, A. C. ABARE, J. E. BOWERS, E. L. HU, S. KELLER and S. P. DENBAARS, *Ibid.* **72** (1998) 1066.
15. J. BAI, T. WANG and S. SAKAI, *J. Appl. Phys.* **88** (2000) 4729.
16. T. WANG, D. NAKAGAWA, M. LACHAB, T. SUGAHARA and S. SAKAI, *Appl. Phys. Lett.* **74** (1999) 3128.
17. D. BIMBERG, M. GRUNDMANN and N. N. LEDENTSOV, Quantum Dot Heterostructures, John Wiley & Sons, Chichester (1999).
18. T. M. HSU, Y. S. LAN, W. H. CHANG, N. T. YEH and J. I. CHYI, *Appl. Phys. Lett.* **76** (2000) 691.
19. W. H. LEE, K. S. KIM, G. M. YANG, C. H. HONG, K. Y. LIM, E. K. SUH, H. J. LEE, H. K. CHO and J. Y. LEE, *J. Korean Physical Society.* **39** (2001) 136.
20. L. T. ROMANO, M. D. MCCLUSKEY, B. S. KRUSOR, D. P. BOUR, C. CHUA, S. BRENNAN and K. M. YU, *J. Crystal Growth* **189/190** (1998) 33.
21. C. C. CHUO, C. M. LEE, T. E. NEE and J. I. CHYI, *Appl. Phys. Lett.* **76** (2000) 3902.
22. Y. S. LIN, K. J. MA, C. HSU, Y. Y. CHUNG, C. W. LIU, S. W. FENG, Y. C. CHENG, M. H. MAO, C. C. YANG, H. W. CHUANG, C. T. KUO, J. S. TSANG and T. E. WEIRICH, *Ibid.* **80** (2002) 2571.
23. F. HOFER, P. WARBICHLER, B. BUCHMAYER and S. KLEBER, *J. Microsc.* **184** (1996) 163.
24. F. HOFER, P. WARBICHER and W. GROGGER, *Ultramicroscopy.* **59** (1995) 15.
25. S. Y. KARPOV, *MRS Internet J. Nitride Semiconductor Res.* **3** (1998) 16.
26. S. W. FENG, Y. Y. CHUNG, C. W. LIU, Y. C. CHENG, C. C. YANG, M. H. MAO, Y. S. LIN, K. J. MA and J. I. CHYI, *Appl. Phys. Lett.* **80** (2002) 4375.

Received 5 October 2004
and accepted 22 July 2005